LAWRENCE
LIVERMORE
NATIONAL
LABORATORY

LLNL-JRNL-827673

Dislocation Theory of Steady and Transient Creep of Crystalline Solids: Predictions for Olivine

T. P. Breithaupt, R. F. Katz, L. N. Hansen, K. M. Kumamoto

October 7, 2021

Proceedings of the National Academy of Sciences

Disclaimer

Dislocation theory of steady and transient creep of crystalline solids: predictions for olivine

Thomas Breithaupt[a,b,1], **Richard F. Katz**,[b], **Lars N. Hansen**[c], **and Kathryn M. Kumamoto**[c,d]

[a]Department of Earth Sciences, University of Cambridge, CB2 3EQ, UK; [b]Department of Earth Sciences, University of Oxford, OX1 3AN, UK; [c]University of Minnesota, Minneapolis, MN, 55455, USA; [d]Lawrence Livermore National Laboratory, CA, 94550, USA

This manuscript was compiled on February 15, 2023

In applications critical to the geological, materials, and engineering sciences, deformation occurs at strain rates too small to be accessible experimentally. Instead, extrapolations of empirical relationships are used, leading to epistemic uncertainties in predictions. To address these problems, we construct a new theory of the fundamental processes affecting dislocations: storage and recovery. We then validate our theory for olivine deformation. This model explains the empirical relationships among strain rate, applied stress, and dislocation density in disparate laboratory regimes. It predicts the previously unexplained dependence of dislocation density on applied stress in olivine. The predictions of our model for Earth conditions differ from extrapolated empirical relationships. For example, it predicts rapid, transient deformation in the upper mantle, consistent with recent measurements of post-seismic creep.

Rheology | Dislocation creep | Transient creep | Dislocation density | Olivine

Many problems in the materials, engineering and geosciences require assessment of the mechanical behaviour of crystalline solids at extremely low strain rates. These include applications to gas turbines (1), power stations (2), glaciers (3), and Earth's interior (4). Understanding the mechanical properties of materials in these settings is crucial for predicting the creep-limited lifetime of engineering components and the response of the solid Earth to changing surface loads, such as shrinking ice sheets. The small strain rates in these settings are impractical or impossible to explore in laboratory experiments. Therefore, predictions are typically made by extrapolation from experiments performed at much higher strain rates. Confidence in such extrapolations should be based on a clear understanding of the physics of deformation. However, steady-state deformation data are largely rationalised using phenomenological power-law fits (5), and transient strain rates are often modelled using approaches that are not rooted in the underlying physics (6). At this point, there is no physics-based model of steady-state and transient deformation that is self-consistent across multiple deformation regimes.

Deformation of crystalline solids occurs by the motion of crystal defects. In this study, we examine the role of line defects—dislocations—within the crystal lattice. Deformation as a consequence of dislocation motion has been divided into categories including low-temperature plasticity, dislocation creep, and grain-size-sensitive dislocation creep, each of which has been modelled as a physically distinct mechanism (e.g., 7). Going beyond these models of steady-state creep, the evolution of dislocation microstructure controls transient strain rates at low strains (8) and other classical features of deformation such as the Hall-Petch effect (9) and the Bauschinger effect (10). Here, we present a unified, physics-based, quantitative description of all these features of deformation associated with dislocation motion.

Deformation due to dislocation motion is sensitive to the density of dislocation lines within crystals. We therefore construct a model for evolution of dislocation density that makes physics-based, testable predictions about deformation at both low and high strain rates. The classical theory for dislocation-density evolution in the materials sciences is the Kocks-Mecking-Estrin (KME) model, which has been used to model low-temperature deformation of metals including silver, copper, aluminium, and nickel (11–16). This theory is derived from the hypothesis that dislocation density increases due to dislocation storage, a geometric description of the increase in dislocation-line length during dislocation glide, and decreases due to dynamic recovery, a description of strain-dependent dislocation annihilation that is thought to dominate at low temperatures (17). However, extensions of the KME model to high temperatures are problematic because they exclude key aspects of dislocation physics, incorporating either phenomenological parameterizations (12, 14) or relying on an empirical scaling between the applied stress and dislocation density (5, 18).

We demonstrate that laboratory data from experiments at low and high temperatures can be explained in a self-consistent manner by accounting for two additional aspects of dislocation physics. First, we augment the KME theory with a model for static recovery that describes the high-temperature, time-dependent annihilation of dislocations. In this model, we

Significance Statement

Many important deformation processes take place at strain rates that are too slow to be investigated experimentally. For example, strain rates in Earth's mantle are typically ten orders of magnitude slower than in the laboratory. To bridge this gap, empirical relationships are extrapolated with large epistemic uncertainties. We propose a model for deformation derived from the microphysics of deformation. In application to olivine, the main mineral of Earth's upper mantle, this model explains for the first time the scaling relationships observed under a range of laboratory conditions. In extrapolation to Earth's mantle, the model predicts a transition in the dominant microphysical processes, leading to predictions distinct from previous studies. For instance, following abrupt stress changes, it predicts rapid transient deformation.

TB designed the study and model with guidance from RFK, LNH, and KMK. All authors discussed results, and wrote and commented on the manuscript.

The authors declare no conflict of interest.

[1]To whom correspondence should be addressed. E-mail: tpb44@cam.ac.uk

emphasise the role of fast-diffusion pathways in dislocation annihilation. Second, we couple the theory of dislocation evolution to a flow law that explicitly describes the competing roles of dislocations as both carriers of deformation and generators of stress fields that act to oppose deformation. The combined model provides a parsimonious, physics-based explanation of (i) yield stresses at low temperatures, (ii) steady-state and transient creep at high temperatures, (iii) the scaling between dislocation density and stress, (iv) kinematic hardening, (v) the Bauschinger effect, and (vi) the Hall-Petch effect.

All of these processes and phenomena are relevant to olivine (6, 7, 10, 19), a mineral that controls the strength of Earth's upper mantle. Olivine has four key advantages in testing our approach. First, its dislocation density can be readily measured using an oxidation-decoration technique (20) and there are many published experiments against which to compare model predictions (19, 21–23). Second, no physics-based model has self-consistently explained the scaling of the steady-state dislocation density with applied stress in olivine, which is empirically distinct from the classical case in which dislocation density is proportional to the applied stress squared (19). Third, recent experiments have demonstrated the crucial importance of modelling dislocation physics in understanding olivine deformation (6, 10), but currently, no self-consistent, physics-based model exists for this purpose. Fourth, there are a variety of independent geophysical observations that constrain the behaviour of Earth's upper mantle at natural strain rates (e.g., 4, 24) that may eventually be used as a test of predictions of our model for strain rates inaccessible in the laboratory.

Model derivation

The two essential components of our model are an equation for the evolution of dislocation density and a flow law that describes how strain rate depends on dislocation density and other variables, such as applied stress. Both are outlined here and detailed in the Supplementary text. Within our framework, we do not distinguish between different types or categories of dislocations.

Dislocation density, ρ, evolves due to dislocation storage and dislocation recovery. Dislocation storage describes the increase in ρ with increasing plastic strain as dislocation loops expand. The storage rate is $\dot{\varepsilon}/(bL)$, where $\dot{\varepsilon}$ is the strain rate, b is the magnitude of the Burgers vector, and L is a length scale that describes the average distance travelled by a dislocation before it is stored in the lattice (16). We assume that L is controlled by the presence of other dislocations and grain boundaries (Supplementary text).

Dislocation recovery describes the decrease in ρ due to dislocation annihilation. Recovery may be characterised as dynamic, whereby its rate is strain-dependent, or as static, whereby its rate is time-dependent. Our model incorporates both types of recovery (Supplementary text); to focus on novel aspects of the model and make connections with high-temperature creep data, we only discuss static recovery here.

In static recovery, dislocations of opposite sign are driven to climb and annihilate by the interaction of their stress fields (25). The rate of recovery depends on the amount of suitable dislocations, their separation, and the climb velocity (25). Dislocation climb requires diffusion of vacancies to the climbing segment of the dislocation. Classical treatments, which assume vacancies diffuse though the lattice, suggest the recovery rate is proportional to ρ^2 (25). However, vacancies can also diffuse along fast diffusion pathways, like dislocation cores and grain boundaries (26, 27). We focus on the role of these fast diffusion pathways and neglect diffusion through the bulk lattice (Supplementary text). To account for different types of pathways, the diffusivities of each type are weighted by the volume fraction of that pathway (28). The volume fraction of dislocation cores (pipes) is proportional to ρ, and hence, the rate of recovery controlled by pipe diffusion is proportional to ρ^3. In contrast, the volume fraction of grain boundaries is inversely proportional to the grain size d, and thus the rate of recovery controlled by grain-boundary diffusion is proportional to ρ^2/d.

Accounting for the rates of dislocation storage and static recovery, the evolution of dislocation density is given by

$$\dot{\rho} = \underbrace{\frac{1}{b}\left(m\sqrt{\rho}+\frac{n}{d}\right)\dot{\varepsilon}}_{\text{storage}} - \underbrace{\left(\mathcal{R}_{\text{gb}}(T)\frac{\rho^2}{d}+\mathcal{R}_{\text{pipe}}(T)\rho^3\right)}_{\text{static recovery}}, \qquad [1]$$

where $\dot{\varepsilon}$ is the strain rate, m and n are material constants, T is the temperature, and $\mathcal{R}_{\times}(T)$ are rate coefficients for static recovery by grain boundary or pipe diffusion. The Arrhenius temperature dependence of these rate coefficients is associated with the diffusivity of the slowest-diffusing species along the respective pathway.

Eq. (1) is coupled to a flow law that describes the dependence of strain rate on dislocation density, applied stress, and temperature. Dislocations are the carriers of deformation, so the flow law depends on dislocation density and velocity (29). Dislocation motion is a thermally-activated process (30) described by a stress-dependent energy barrier (Supplementary text), which leads to the flow law

$$\dot{\varepsilon} = A(T)\rho\sinh\left(\frac{\sigma-\sigma_\rho-\sigma_d}{\sigma_{\text{ref}}(T)}\right), \qquad [2]$$

where $A(T)$ is a rate coefficient with an Arrhenius dependence on temperature, and σ is the applied stress. $\sigma_{\text{ref}}(T)$ is the reference stress, which is related to the strength of barriers to dislocation motion and has a linear dependence on temperature (Supplementary text).

Through thermodynamic considerations, we find that the applied stress is opposed by two microstructurally-derived stresses, σ_ρ and σ_d (Supplementary text). The classical Taylor stress, $\sigma_\rho = \alpha\mu b\sqrt{\rho}$, describes the cumulative effect of stress fields generated by dislocations (31). Here, μ is the shear modulus and α is a constant. The second, $\sigma_d = \beta\mu b/d$, is the threshold stress, which classically represents the minimum applied stress required for a dislocation loop to expand within a grain (32), where β is a constant. In traditional models of dislocation creep, the dislocation velocity is assumed to be limited by the timescale of dislocation climb (e.g., 33). In contrast, within our framework, we self-consistently model the effect of dislocation climb on dislocation velocity through its influence on dislocation density. Slower dislocation climb leads to a higher dislocation density, and therefore a higher Taylor stress, which opposes the applied stress driving deformation in Eq. 2 and thereby limits the dislocation velocity.

Eq. (1) and Eq. (2) constitute our model for deformation due to dislocations at high temperature. The model incorporates the physics of both dislocation climb, through the

recovery terms in Eq. (1), and dislocation glide, in the form of the flow law (Eq. (2)). The full model, detailed in the supplementary text, self-consistently describes transient and steady-state deformation at both low and high temperatures and incorporates grain-size effects. Given the applied stress, temperature, and grain size, these equations can be solved for the evolution of dislocation density and strain rate, both prior to and at steady state.

Model validation and calibration

Before the model can be applied, it must be calibrated and validated by comparison with data derived from deformation experiments. To this end, we use published data from steady-state (Figure 1) and transient (Figure 2) creep experiments on olivine.

At steady state, the model predicts a (nonlinear) relationship among stress, dislocation density, and strain rate. This relationship is modulated by the grain size that, for simplicity, we treat as an independent variable, though in fact grain-size evolution may be coupled to dislocation density (e.g., 36). We do not consider oxygen fugacity, which is known to affect strain rates (34). Since fugacity varies among experiments, we only consider data collected at the Ni–NiO buffer. Our calibration and subsequent extrapolation to mantle conditions are not particularly sensitive to differences among activation energies of different processes; we therefore assume that all temperature-dependent processes have the same activation energy, Q.

We first test the hypothesis that pipe diffusion plays a critical role in grain-size insensitive dislocation creep in olivine. To do so, we assume grain-boundary diffusion is negligible and calibrate our model against the steady-state experimental data on large-grained (0.9 mm) aggregates from Keefner et al. (34). This calibration constrains the rate coefficients of the flow law (Eq. (2)) and pipe-diffusion recovery (Eq. (1)), as well as the activation energy.

Figure 1A demonstrates that the model captures the stress and temperature dependence of strain rate. To highlight the stress dependence of strain rate, we normalise the data to one temperature using our fitted activation energy in the inset of Figure 1A. Although our model is not formally a power law, it gives an apparent power law exponent of $\sim$3.5 over the range of laboratory conditions, consistent with previous empirical analysis of this dataset (34).

Figure 1B compares the predicted steady-state dislocation density with published measurements from experiments using single crystals of olivine (21–23). At intermediate applied stresses (30–400 MPa), the model predicts that the dislocation density approximates a power law of applied stress with an exponent of 1.4, consistent with an empirical power-law fit (22). However, at both small and large applied stress, the model predicts that dislocation density has a stronger dependence on applied stress, consistent with the trend of experimental data at small applied stresses and the more-limited data at large applied stresses. Aside from α, which relates the Taylor stress to the dislocation density, all parameters used to predict dislocation density are constrained by the calibration in Figure 1A. The data in Figure 1B constrains α to be 2.46 ± 0.13 (Supplementary text). We note that the value of α only shifts the predicted dislocation-density curve in Figure 1B to lower or higher dislocation density without affecting its shape.

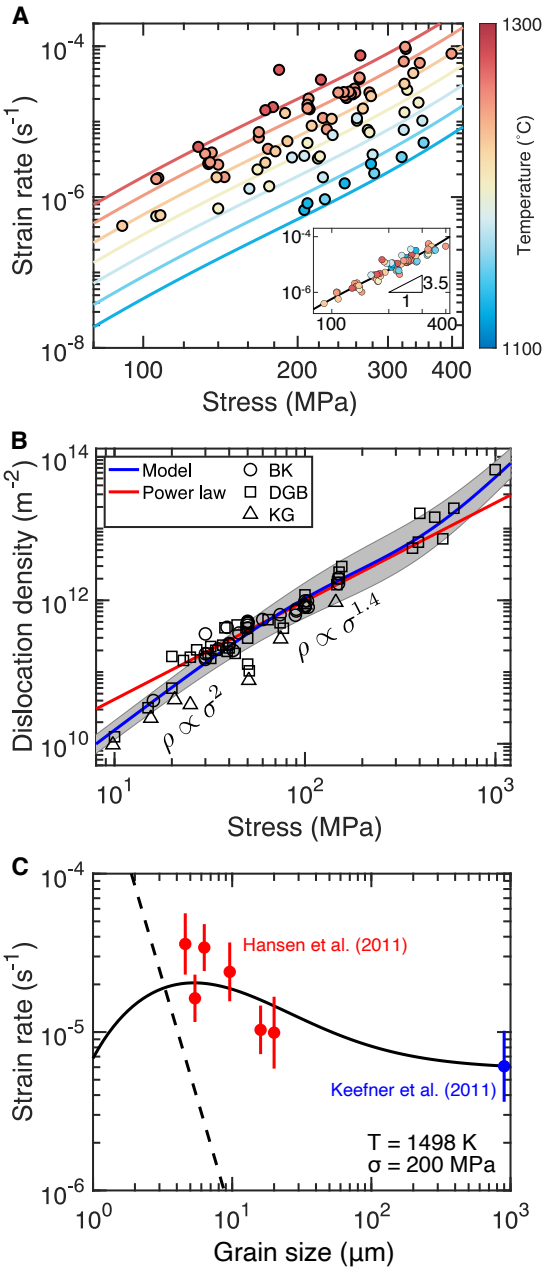

Fig. 1. Model predictions for steady-state deformation at laboratory conditions compared to experimental data. A. Strain rate as a function of applied stress predicted by our calibrated model, assuming that grain-size effects are negligible (solid lines). The mechanical data from Keefner et al. (34) used in the calibration are plotted for comparison (circles) at different temperatures (indicated by colour). The inset compares model prediction at T = 1498 K with data normalised to this temperature. B. Dislocation density as a function of stress predicted by the calibrated model plotted in A (blue line) compared to an empirical dislocation-density piezometer (22) (red line) and experimental data (black open symbols). The grey shaded area represents the 95% confidence interval from propagating the uncertainties in the underlying model parameters. Data are taken from experiments on single crystals (BK = (22), DGB = (21), KG = (23)). C. Strain rate as a function of grain size predicted by the calibrated model incorporating grain-size effects (solid line) compared to normalised mechanical data from Keefner et al. (34) (blue) and Hansen et al. (35) (red). The experimental data are normalised to a temperature of 1498 K and a stress of 200 MPa and then then grouped according to grain size. The circles represent the mean normalised strain rate within each group. The error bars represent one standard deviation of the normalised strain rate within each group. The strain rate predicted by the diffusion creep flow law from (35) is plotted as a dashed line.

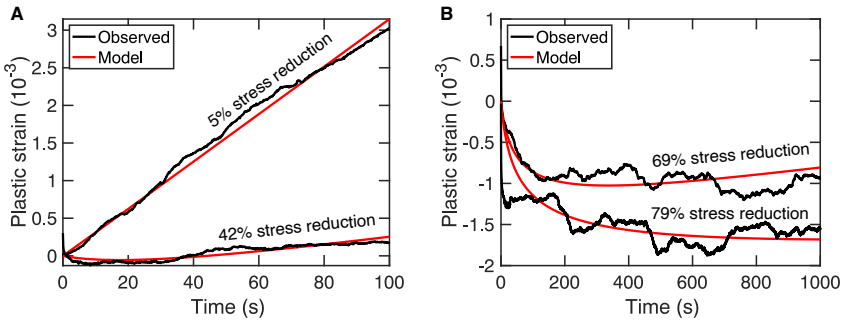

Fig. 2. Comparison of transient deformation predicted by our model to experimental data. Plastic strain as a function of time from a stress reduction experiment (OxR0002) from Hansen et al. (6) (black line) compared to the model prediction (red line). This experiment was performed on a single crystal compressed uniaxially in the $[101]_c$ orientation at 1523 K. The initial stress prior to reduction was 162 MPa. The curves are labelled with the percentage reduction in stress. In A, the plastic strain rate evolves over relatively short timescales (∼10 seconds), whereas in B, the plastic strain rate evolves over longer timescales (∼100 seconds).

We next calibrate the full model, including grain size effects, against experimental data from Hansen et al. (35) and Keefner et al. (34). The former used fine-grained (≈ 10 µm) olivine aggregates. This calibration constrains the rate coefficients of the flow law (Eq. (2)) and both types of recovery (Eq. (1)), as well as the activation energy. Figure 1C compares the predicted grain-size dependence of strain rate against the experimental data. The experimental data are normalised to a single stress and temperature using the calibrated model. The calibrated model captures the stress, temperature, and grain-size dependencies of both datasets.

Finally, we consider the transient deformation predicted by our model. Hansen et al. (6) performed stress-reduction experiments in which olivine single crystals are deformed at a constant applied stress until steady-state deformation is achieved, and then the applied stress is reduced to a new constant value. Transient deformation occurs after each stress step. We calibrate our model for single crystal deformation using steady-state mechanical data from Hansen et al., treating the steady-state Taylor stress prior to stress reduction as a fitting parameter (see supplementary text). Figure 2 demonstrates that our model provides a good fit to the transient plastic strain. Small stress reductions ($< 50\%$) lead to short transients, whereas larger stress reductions result in longer transients that have extended periods of reverse plastic strain rates. Importantly, our model is able to match the sense of the transient, in terms of forward or reverse plastic strain, as well as the magnitude of reverse plastic strain following the transient. In our model, the negative plastic strain rates result from the Taylor stress temporarily exceeding the (positive) applied stress, consistent with the Bauschinger effect.

Deformation in the laboratory

Our model elucidates the microphysical relationships between dislocation density, applied stress, and strain rate that operate at laboratory conditions. The model illustrates that the steady-state dislocation density may be limited either by the Taylor stress or by recovery. In the first case, dislocation density increases until the Taylor stress approximately balances the applied stress, such that $\rho \propto \sigma^2$ and the strain rate becomes small. As a result, the dislocation storage rate becomes small and can balance the recovery rate. Alternatively, at steady state, the applied stress may significantly exceed the Taylor stress if dislocation density is limited instead by recovery. If recovery occurs mainly by pipe diffusion, the model predicts $\rho \propto \sigma^{2/3}$. The calibrated model predicts that, at laboratory conditions, both processes are significant, leading to the apparent $\rho \propto \sigma^{1.4}$ scaling observed in experimental data (Figure 1B). This scaling previously lacked a physical explanation.

The ρ–σ scaling also influences the relationship between steady-state strain rate and applied stress. The steady-state strain rate is not linearly proportional to dislocation density as classically suggested by the Orowan equation (Supplementary text) because the Taylor stress is also dependent on the dislocation density. The precise relationship between steady-state strain rate and dislocation density can be determined by solving Eq. (1) at steady state. If pipe-diffusion rate-limits dislocation climb, and thereby dislocation recovery, then $\dot{\varepsilon}_{ss} \propto \rho^{5/2}$. Combining this scaling for strain rate with the scaling between dislocation density and applied stress at laboratory conditions, we predict an apparent stress exponent of $(5/2) \times 1.4 = 3.5$, in agreement with experimental data on coarse-grained olivine (Figure 1A).

Accounting for grain-boundary processes results in a model that is sensitive to grain size, as illustrated in Figure 1C. Grain size influences the steady-state dislocation density, and therefore strain rate, through recovery controlled by grain-boundary diffusion. Decreasing the grain size increases the rate of recovery, causing a corresponding decrease in the steady-state dislocation density and hence Taylor stress. At larger grain sizes, the strain rate is limited by the Taylor stress and hence the steady-state strain rate increases with decreasing grain size. However, at smaller grain sizes, the strain rate is instead limited by the availability of dislocations, and hence further decreasing the grain size decreases the strain rate. At constant applied stress, the dependence of the steady-state strain rate on dislocation density can be understood through Eq. (2), which has a maximum as a function of dislocation density.

These grain size dependencies are consistent with available experimental data. For fine-grained samples (∼10's µm) and laboratory-accessible stresses, our model predicts an inverse relationship between strain rate and grain size (Figure 1C) and an approximate stress exponent of 3, congruent with empirical analyses (35). These data were previously interpreted in terms of dislocation-accommodated grain-boundary sliding (disGBS). In this interpretation, strain rate is limited by dislocation annihilation at grain boundaries (37, 38). This rate-limiting process is the same as the case considered here in which grain-boundary diffusion controls dislocation recovery. In classic models of disGBS, there is an additional contribution to strain rate from sliding on grain boundaries, which we do not model. However, sliding is understood to make a limited contribution (1 to 10%) towards the total strain rate (39), justifying the omission of this process from our model. We note that recovery by grain-boundary diffusion has the same functional form as

recovery due to grain-boundary migration, highlighting an additional link to models focused on migration as a recovery mechanism (36).

Deformation at geological strain rates

We have thus far demonstrated consistency between our model and experiments. We now examine predictions of our model beyond laboratory conditions. In particular, we consider applied stresses far smaller than those normally accessed in the laboratory but typical within Earth's mantle. Figure 3A explores the predicted dependence of strain rate on applied stress for a range of grain sizes. In the limit of infinite grain size, for which grain-boundary diffusion does not contribute to recovery, we predict a transition in stress exponent from 3.5 at typical laboratory stresses to 5 at smaller applied stresses. The transition in stress exponent results from a transition in the ρ–σ relationship.

As noted above, at small applied stresses we predict $\rho \propto \sigma^2$ due to the reduced recovery rates associated with pipe diffusion. The recovery rate controls the difference between the applied stress and Taylor stress. At small applied stresses, the recovery rate becomes disproportionately small, such that the Taylor stress is approximately equal to the applied stress, resulting in the $\rho \propto \sigma^2$ scaling (Figure 1B). Therefore, the apparent stress exponent is given by $(5/2) \times 2 = 5$. The range of predicted stress exponents for dislocation creep is consistent with the range of stress exponents observed in single-crystal deformation experiments performed on olivine, for which the stress exponent across experiments varied between 3 and 5 (42).

At finite grain size, the predicted steady-state strain rate curves in Figure 3A have a complex relationship with the applied stress and grain size. Our model at steady-state can be simplified by assuming the applied stress balances the sum of the Taylor and threshold stresses, which approximately holds in Figure 3A. Combining this balance with Eq. (1) and Eq. (2) yields $\dot{\varepsilon}_{ss} \propto (\sigma - \sigma_d)^4(\sigma_d/\sigma)$. This approximate flow law has two limits. In the limit that $\sigma \gg \sigma_d$, we recover an apparent stress exponent of 3 and a grain size exponent of 1, consistent with observations in the laboratory (35). In the limit that $\sigma \to \sigma_d$, $\dot{\varepsilon} \to 0$ such that the threshold stress σ_d acts as a yield stress that is inversely proportional to the grain size, which is consistent with recent evaluations of the Hall-Petch effect (9).

The predicted scalings in Figure 3A illustrate an important point. The measured power-law exponents describing relationships between steady-state strain rates, applied stresses, grain size, and dislocation density are not necessarily intrinsic properties of deformation mechanisms in a given material. Instead, empirical exponents reflect the underlying balance in microphysical processes at laboratory conditions. Therefore, exponents measured in the laboratory do not necessarily apply outside of these conditions, even though the same set of microphysical processes operate. Consequently, power laws fitted at laboratory conditions should only be extrapolated with extreme care. Furthermore, although we have only considered the effect of grain size and applied stress, the same considerations also apply to other state variables such as oxygen fugacity, water fugacity, and silica activity.

Figure 3B is a deformation-mechanism map exploring strain rate as a function of applied stress and grain size. We compare

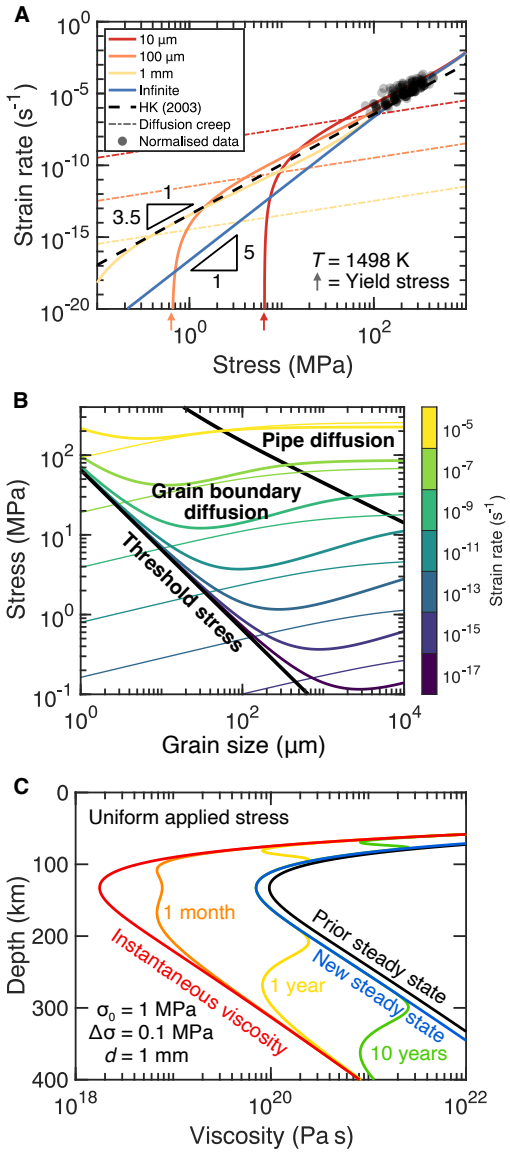

Fig. 3. The predictions of our calibrated model for deformation at geologic conditions. A. Strain rate as a function of stress at a temperature of 1498 K. Curves are constructed from the calibrated model incorporating grain-size effects using grain sizes of 10 µm, 100 µm, and 1 mm, and from the calibrated model that neglects grain-size effects (infinite). Experimental data (black circles) from Keefner et al. (34) and Hansen et al. (35) are normalised to the same temperature using the fitted activation energy. Plotted for comparison are the dislocation creep flow law (black dashed) from Hirth and Kohlstedt (7), and the diffusion creep flow law (coloured dot-dashed) from Hansen et al. (35). The yield stresses for dislocation deformation are indicated by arrows below the stress axis. B. Deformation mechanism map of dislocation-accommodated deformation. The map is constructed as a function of grain size and stress at a temperature of 1498 K. Contours represent constant strain rate. Thick contours represent the strain rate predicted by our model and the thin contours are calculated using a combination of the dislocation creep flow law from Hirth and Kohlstedt (7) and the grain-size sensitive dislocation creep flow law from Hansen et al. (35). The colours of the contours indicate the strain rate. The threshold stress and the boundary between the different dominant recovery mechanisms (pipe diffusion and grain boundary diffusion) are plotted as thick black lines. C. Viscosity as a function of depth predicted by our model assuming a mantle grain size of 1 mm. The initial steady-state viscosity under a uniform stress of 1 MPa is plotted as a black line. The coloured lines indicate the viscosity following a 0.1 MPa increase in stress for a variety of times (red = instantaneous, orange = 1 month following, yellow = 1 year following, green=10 years following, blue = new steady state). The temperature as a function of depth is calculated assuming a half-space cooling model and an adiabatic geotherm for a 50 million-year-old lithosphere with a potential temperature of 1350°C (40, pp. 185–187). The activation volume is assumed to be 15 cm^3/mol in keeping with Dixon and Durham (41).

predicted strain rates to those derived from previous flow laws for dislocation creep (7) and grain-size sensitive dislocation creep (35). At typical laboratory strain rates ($\geq 10^{-5}\,\mathrm{s}^{-1}$), the predictions of our calibrated model are in agreement with the previous flow laws. However, at mantle stresses (~ 1 MPa) and grain sizes ($\sim$3 mm) (19), the predicted strain rates are approximately an order of magnitude smaller than previous flow laws for dislocation deformation (7, 35). The difference in the predicted strength of the mantle reflects the changes in the scalings of strain rate with applied stress and grain size predicted by our model outside of laboratory conditions. Indeed, our model predicts that deformation has a range of grain-size sensitivities, including both weakening and strengthening with decreasing grain size. Despite these differences, we find that our model at $d = 1$ mm and mantle stresses makes similar predictions to the Hirth and Kohlstedt (7) dislocation creep flow law (Figure 3A). This correspondence may explain the successful application of this dislocation creep flow law to geophysical models (e.g., 43). Finally, a significant region of the deformation mechanism map corresponds to no deformation at all by dislocation-mediated mechanisms. In this region, stresses are lower than the threshold stress, although we note that typical mantle stresses and grain sizes lie outside this region. Deformation in this region is accommodated by other deformation mechanisms such as diffusion creep. The predictions of the diffusion creep flow law from Hansen et al. (35) are compared to our model in Figure 3A. The higher strain rates at low applied stress associated with high-temperature diffusion creep would obscure the yielding behaviour predicted by our model.

Transient deformation at geological conditions

Next, we consider the predictions of our model for time-dependent mantle deformation. Figure 3C explores how an abrupt change in applied stress affects deformation at mantle conditions. We assume an initially uniform differential stress of 1 MPa, a reasonable ambient differential stress for the mantle (44). For this stress, the steady-state viscosity at 100 km depth is $\approx 10^{20}$ Pa s. Although the stress changes in realistic geodynamic processes will be spatially and temporally variable, in this simplified example we apply a uniform stress change instantaneously, a value consistent with stress changes inferred from models of post-seismic creep (45). Although both the old and new steady-state viscosities are similar, the transient viscosities differ significantly from the steady state. Instantaneously, the viscosity drops by approximately two orders of magnitude (to $\approx 10^{18}$ Pa s at 100 km depth) and evolves over a timescale of months to years.

The large viscosity reduction instantaneously following a change in stress in Figure 3C can be understood by examining Eq. (2). At the instant of the stress change, the dislocation density is unchanged. Consequently, any change in viscosity must be controlled by the change in the net stress driving dislocation motion, which we term the effective stress. The ratio of viscosities immediately following (η^+) and prior to (η^-) the stress change are approximately given by

$$\frac{\eta^+}{\eta^-} \approx \frac{\sigma^-_{\mathrm{eff}}}{\sigma^-_{\mathrm{eff}} + \Delta\sigma}, \qquad [3]$$

where $\Delta\sigma$ is the stress change and $\sigma^-_{\mathrm{eff}} = \sigma^- - \sigma_\rho - \sigma_d$ is the effective stress prior to the stress change. At laboratory conditions, such as those considered in Figure 2, the effective stress is inferred to be comparable in magnitude to the applied stress. As a result, stress changes will not drive disproportionate changes in the viscosity in laboratory experiments. However, at geological conditions, we predict that the steady-state effective stress is much smaller in magnitude than the applied stress, and thus stress changes can drive disproportionate changes in the viscosity. Indeed, in Figure 3C, the effective stress is predicted to be of order of kPa, which is two orders of magnitude smaller than the stress change considered, and thus the instantaneous transient viscosity is approximately two orders of magnitude smaller than the prior steady-state viscosity.

The magnitude of the reduction in viscosity and the evolution timescale are consistent with geophysical observations of processes associated with abrupt stress changes, such as post-seismic creep (24, 43, 46) and crustal uplift in response to ongoing recent anthropogenic ice loss across a number of regions (e.g., 47–50). The ratio of instantaneous to steady-state viscosity is approximately independent of depth, a prediction that is in striking agreement with viscosity profiles inverted from surface displacements after earthquakes (45). The rate of evolution towards steady state is depth dependent. Depths with smaller absolute transient viscosities, and therefore larger strain rates, evolve more quickly, indicating that dislocation storage controls the transient evolution of viscosity at mantle conditions. Thus, whilst steady-state deformation at mantle stresses is controlled by the recovery coefficients $\mathcal{R}_\times(T)$, transient deformation is sensitive to the flow law coefficient $A(T)$.

Transient, dislocation-accommodated deformation in Earth is commonly modelled using a nonlinear Burgers model, in which transient and steady-state viscosities possess the same sensitivity to the applied stress (e.g., 6), and references therein). However, our results indicate that transient and steady-state viscosities have a fundamentally different dependence on the applied stress. Moreover, our results demonstrate that transient and steady-state viscosities at mantle conditions are likely controlled by separate components of the dislocation microphysics. In this work, we have considered the effect of dislocation density on transient deformation. Over comparable strains, transient deformation may also be influenced by other factors, such as the development of inter-granular stress heterogeneity (e.g., 51). However, models of this mechanism (51) assume non-linear transient rheological laws that are in disagreement with laboratory observations, in which the initial strain-rates immediately following stress changes are a linear function of the new stress (6). Over larger strains than investigated here, the evolution of other aspects of microstructure that we do not account for, such as grain size and crystallographic texture, will also influence the transient viscosity (52). Therefore, we suggest the evolution of dislocation density is the most relevant process for predicting transient viscosity during stress changes that occur on human timescales, such as post-seismic creep and crustal uplift in response to recent anthropogenic ice loss.

Broader implications

Although we have calibrated our model for olivine deformation, our formulation is applicable to a broad array of materials. Whilst the predicted transitions in stress exponent have not

been directly observed in olivine, such transitions have been observed in solid-solution alloys (53), some of which have already been found to be good analogs for olivine (54). For example, in experiments on an Al–Mg alloy, the apparent stress exponent decreases from 5 to 3 for applied stresses above 7 MPa (55). This transition in stress exponent is correlated with a change in the scaling of an empirically-observed back stress opposing deformation, which we take to be the Taylor stress in our model. At the smallest stresses, for which the stress exponent is 5, the back stress is observed to be approximately equal to the applied stress, whereas at higher stresses, the back stress is a fraction of the applied stress (55). These observations are in agreement with the predictions of our model for olivine. We believe that this agreement underlines the importance of constructing microphysical models of deformation to make physics-based predictions at conditions far from the laboratory.

The calibrated model that we have presented provides a quantitative description of dislocation creep, grain-size-sensitive dislocation creep, and the Hall-Petch effect in olivine. The model is in agreement with observations of transient strain obtained from stress-reduction tests and is in broad agreement with estimated transient viscosities from recent observations of geophysical processes associated with abrupt stress changes. Our model is easily extended to incorporate dynamic recovery (Supplementary text), the dominant dislocation annihilation process at low temperatures. Indeed, our formulation of this process, is consistent with that used by Hansen et al. (10) to model strain hardening and the Bauschinger effect at low temperatures. As a result, our model also extends to deformation by low-temperature plasticity. In this work, we have assumed that the activation energies of all processes are equal. Future work will constrain the potentially different activation energies of each process.

ACKNOWLEDGMENTS. T.B. was supported by a Natural Environment Research Council (NERC NE/L002612/1) studentship in the Oxford NERC Doctoral Training Partnership, and by a Research Fellowship from the Royal Commission for the Exhibition of 1851. K.M.K. was supported by National Science Foundation grant EAR-1806791. L.N.H. and K.M.K. were supported by National Science Foundation grant EAR-2022433. This research received funding from the European Research Council under Horizon 2020 research and innovation program grant agreement number 772255. Lawrence Livermore National Laboratory is operated by Lawrence Livermore National Security, LLC, for the U.S. Department of Energy, National Nuclear Security Administration under Contract DE-AC52-07NA27344. LLNL-JRNL-827673.

1. M Whittaker, W Harrison, R Lancaster, S Williams, An analysis of modern creep lifing methodologies in the titanium alloy ti6-4. *Mater. Sci. Eng. A* **577**, 114–119 (2013).
2. B Wilshire, P Scharning, Prediction of long term creep data for forged 1cr–1mo–0· 25v steel. *Mater. science technology* **24**, 1–9 (2008).
3. BM Minchew, CR Meyer, AA Robel, GH Gudmundsson, M Simons, Processes controlling the downstream evolution of ice rheology in glacier shear margins: case study on rutford ice stream, west antarctica. *J. Glaciol.* **64**, 583–594 (2018).
4. L Pan, et al., Rapid postglacial rebound amplifies global sea level rise following west antarctic ice sheet collapse. *Sci. Adv.* **7**, eabf7787 (2021).
5. S Spigarelli, R Sandström, Basic creep modelling of aluminium. *Mater. Sci. Eng. A* **711**, 343–349 (2018).
6. LN Hansen, D Wallis, T Breithaupt, CA Thom, I Kempton, Dislocation creep of olivine: Back-stress evolution controls transient creep at high temperatures. *J. Geophys. Res. Solid Earth* **126**, e2020JB021325 (2021).
7. G Hirth, D Kohlstedt, Rheology of the upper mantle and the mantle wedge: A view from the experimentalists. *Geophys. Monogr. Geophys. Union* **138**, 83–106 (2003).
8. W Blum, P Eisenlohr, F Breutinger, Understanding creep—a review. *Metall. Mater. Transactions A* **33**, 291–303 (2002).
9. D Dunstan, A Bushby, Grain size dependence of the strength of metals: The hall–petch effect does not scale as the inverse square root of grain size. *Int. J. Plast.* **53**, 56–65 (2014).
10. LN Hansen, et al., Low-temperature plasticity in olivine: Grain size, strain hardening, and the strength of the lithosphere. *J. Geophys. Res. Solid Earth* **124**, 5427–5449 (2019).
11. U Kocks, A statistical theory of flow stress and work-hardening. *Philos. Mag.* **13**, 541–566 (1966).
12. UF Kocks, Laws for Work-Hardening and Low-Temperature Creep. *J. Eng. Mater. Technol.* **98**, 76–85 (1976).
13. U Essmann, H Mughrabi, Annihilation of dislocations during tensile and cyclic deformation and limits of dislocation densities. *Philos. Mag. A* **40**, 731–756 (1979).
14. H Mecking, U Kocks, Kinetics of flow and strain-hardening. *Acta Metall.* **29**, 1865–1875 (1981).
15. Y Estrin, H Mecking, A unified phenomenological description of work hardening and creep based on one-parameter models. *Acta Metall.* **32**, 57–70 (1984).
16. Y Estrin, Dislocation theory based constitutive modelling: foundations and applications. *J. Mater. Process. Technol.* **80**, 33–39 (1998).
17. W Nix, J Gibeling, D Hughes, Time-dependent deformation of metals. *Metall. Transactions A* **16**, 2215–2226 (1985).
18. R Sandström, J Hallgren, The role of creep in stress strain curves for copper. *J. nuclear materials* **422**, 51–57 (2012).
19. G Hirth, D Kohlstedt, The stress dependence of olivine creep rate: Implications for extrapolation of lab data and interpretation of recrystallized grain size. *Earth Planet. Sci. Lett.* **418**, 20–26 (2015).
20. D Kohlstedt, C Goetze, W Durham, J Vander Sande, New technique for decorating dislocations in olivine. *Science* **191**, 1045–1046 (1976).
21. W Durham, C Goetze, B Blake, Plastic flow of oriented single crystals of olivine: 2. observations and interpretations of the dislocation structures. *J. Geophys. Res.* **82**, 5755–5770 (1977).
22. Q Bai, D Kohlstedt, High-temperature creep of olivine single crystals, 2. dislocation structures. *Tectonophysics* **206**, 1–29 (1992).
23. D Kohlstedt, C Goetze, Low-stress high-temperature creep in olivine single crystals. *J. Geophys. Res.* **79**, 2045–2051 (1974).
24. AM Freed, G Hirth, MD Behn, Using short-term postseismic displacements to infer the ambient deformation conditions of the upper mantle. *J. Geophys. Res. Solid Earth* **117** (2012).
25. W Blum, Role of dislocation annihilation during steady-state deformation. *Phys. Status Solidi (b)* **45**, 561–571 (1971).
26. J Spingarn, D Barnett, W Nix, Theoretical descriptions of climb controlled steady state creep at high and intermediate temperatures. *Acta Metall.* **27**, 1549–1561 (1979).
27. J Spingarn, W Nix, A model for creep based on the climb of dislocations at grain boundaries. *Acta Metall.* **27**, 171–177 (1979).
28. E Hart, On the role of dislocations in bulk diffusion. *Acta Metall.* **5**, 597 (1957).
29. E Orowan, Zur kristallplastizität. i. *Zeitschrift für Physik* **89**, 605–613 (1934).
30. A Krausz, A rate theory of dislocation mobility. *Acta Metall.* **16**, 897–902 (1968).
31. GI Taylor, The mechanism of plastic deformation of crystals. part i.—theoretical. *Proc. Royal Soc. London. Ser. A, Containing Pap. a Math. Phys. Character* **145**, 362–387 (1934).
32. TT Gribb, RF Cooper, Low-frequency shear attenuation in polycrystalline olivine: Grain boundary diffusion and the physical significance of the andrade model for viscoelastic rheology. *J. Geophys. Res. Solid Earth* **103**, 27267–27279 (1998).
33. Si Karato, Deformation of earth materials. *An introduction to rheology Solid Earth* **463** (2008).
34. J Keefner, S Mackwell, D Kohlstedt, F Heidelbach, Dependence of dislocation creep of dunite on oxygen fugacity: Implications for viscosity variations in earth's mantle. *J. Geophys. Res. Solid Earth* **116** (2011).
35. L Hansen, M Zimmerman, DL Kohlstedt, Grain boundary sliding in san carlos olivine: Flow law parameters and crystallographic-preferred orientation. *J. Geophys. Res. Solid Earth* **116** (2011).
36. J Platt, W Behr, Grainsize evolution in ductile shear zones: Implications for strain localization and the strength of the lithosphere. *J. Struct. Geol.* **33**, 537–550 (2011).
37. T Langdon, A unified approach to grain boundary sliding in creep and superplasticity. *Acta metallurgica et materialia* **42**, 2437–2443 (1994).
38. F Ferreira, LN Hansen, K Marquardt, The effect of grain boundaries on plastic deformation of olivine. *J. Geophys. Res. Solid Earth* **126**, e2020JB020273 (2021).
39. TG Langdon, Grain boundary sliding revisited: Developments in sliding over four decades. *J. Mater. Sci.* **41**, 597–609 (2006).
40. DL Turcotte, G Schubert, *Geodynamics*. (Cambridge university press), pp. 185–187 (2002).
41. NA Dixon, WB Durham, Measurement of activation volume for creep of dry olivine at upper-mantle conditions. *J. Geophys. Res. Solid Earth* **123**, 8459–8473 (2018).
42. Q Bai, S Mackwell, D Kohlstedt, High-temperature creep of olivine single crystals 1. mechanical results for buffered samples. *J. Geophys. Res. Solid Earth* **96**, 2441–2463 (1991).
43. AM Freed, R Bürgmann, Evidence of power-law flow in the mojave desert mantle. *Nature* **430**, 548–551 (2004).
44. L Kohlstedt, L Hansen, Constitutive equations, rheological behavior, and viscosity of rocks, in "mineral physics"(ed. price, gd, stixrude, l.), treatise on geophysics, 2 (2015).
45. JR Weiss, et al., Illuminating subduction zone rheological properties in the wake of a giant earthquake. *Sci. advances* **5**, eaax6720 (2019).
46. AM Freed, R Bürgmann, E Calais, J Freymueller, S Hreinsdóttir, Implications of deformation following the 2002 denali, alaska, earthquake for postseismic relaxation processes and lithospheric rheology. *J. Geophys. Res. Solid Earth* **111** (2006).
47. VR Barletta, et al., Observed rapid bedrock uplift in amundsen sea embayment promotes ice-sheet stability. *Science* **360**, 1335–1339 (2018).
48. SA Khan, et al., Geodetic measurements reveal similarities between post–last glacial maximum and present-day mass loss from the greenland ice sheet. *Sci. advances* **2**, e1600931 (2016).
49. A Richter, et al., Crustal deformation across the southern patagonian icefield observed by gnss. *Earth Planet. Sci. Lett.* **452**, 206–215 (2016).
50. CF Larsen, RJ Motyka, JT Freymueller, KA Echelmeyer, ER Ivins, Rapid viscoelastic uplift in southeast alaska caused by post-little ice age glacial retreat. *Earth planetary Sci. letters* **237**,

548–560 (2005).
51. Si Karato, A theory of inter-granular transient dislocation creep: Implications for the geophysical studies on mantle rheology. *J. Geophys. Res. Solid Earth* **126**, e2021JB022763 (2021).
52. L Hansen, M Zimmerman, D Kohlstedt, Laboratory measurements of the viscous anisotropy of olivine aggregates. *Nature* **492**, 415–418 (2012).
53. P Yavari, TG Langdon, An examination of the breakdown in creep by viscous glide in solid solution alloys at high stress levels. *Acta metallurgica* **30**, 2181–2196 (1982).
54. RF Cooper, DS Stone, T Plookphol, Load relaxation of olivine single crystals. *J. Geophys. Res. Solid Earth* **121**, 7193–7210 (2016).
55. H Oikawa, K Sugawara, S Karashima, Creep behavior of al-2.2 at% mg alloy at 573 k. *Transactions Jpn. Inst. Met.* **19**, 611–616 (1978).

PNAS
www.pnas.org

Supplementary Information for

Dislocation theory of steady and transient creep of crystalline solids: predictions for olivine

Thomas Breithaupt, Richard F. Katz, Lars N. Hansen, Kathryn M. Kumamoto

Thomas Breithaupt.
E-mail: tpb44@cam.ac.uk

This PDF file includes:

Supporting Information Text

Derivation of model. Our theoretical framework comprises a model for the evolution of dislocation density and a flow law that relates strain rate to dislocation density and applied stress. We consider each of these below, in turn. Although stress and strain rate are, in general, tensor quantities, we treat both as scalars; we are not considering the effects of anisotropy and use data from uniaxial deformation experiments. Furthermore, we make the simplifying assumption that dislocation density may be treated single, scalar variable. Consequently we do not distinguish between the densities of dislocations associated with individual slip systems or categories of dislocations such as geometrically-necessary, statistically-stored, mobile and immobile. We do not model grain-size evolution, rather we treat grain size as a model parameter.

Dislocation density evolution. Our model of dislocation-density evolution quantifies several processes that affect the density of dislocations. These include terms that act to increase dislocation density (storage) and those that decrease dislocation density (dislocation annihilation through dynamic and static recovery). We assume that each process operates independently of the others and hence that the total rate of change of dislocation density is the linear combination of the separate rates,

$$\dot{\rho}_{\text{total}} = \dot{\rho}_{\text{storage}} - \dot{\rho}_{\text{dynamic}} - \dot{\rho}_{\text{static}}. \quad [1]$$

The rates of dislocation storage and dynamic recovery are modelled according to the Mecking and Kocks model (1). We complement this approach with the rate of static recovery, with an emphasis on the role of fast diffusion pathways.

We model increases in dislocation density by dislocation storage, a process first described by Kocks (1–5). Consequently, we do not model the operation of dislocation sources. Dislocation storage accounts for a geometrical property of dislocation glide; as dislocations glide, their total line length increases (2). There is a corresponding increase in dislocation density because dislocation density is the total dislocation line length per unit volume. In contrast, the strain produced by dislocation motion is proportional to the area swept by the dislocation. Consequently, the rate of change of dislocation density with strain is inversely proportional to the lateral extent of the dislocation loops. An illustrative example is given by an expanding circular dislocation loop (6). The strain associated with the loop is proportional to the area swept by the loop as it expands (πr^2), whereas the dislocation density is proportional to the perimeter of the loop ($2\pi r$). As a result, $\Delta\rho/\Delta\varepsilon \propto 2/r$.

Dislocation storage is parameterised statistically, using the dislocation mean free path Λ, the distance travelled by a gliding dislocation before it is obstructed and ceases motion (1, 3–5). The rate of dislocation storage is

$$\dot{\rho}_{\text{storage}} = \frac{1}{b\Lambda}\dot{\varepsilon}, \quad [2]$$

where b is the magnitude of the Burgers vector (1, 3–5). There are several microstructural features that obstruct dislocation motion and thus control the mean free path (4, 5). Here we consider two such obstacles: grain boundaries and other dislocations. If grain boundaries act to impede dislocation motion, then $\Lambda \propto d$, where d is the grain size. If other dislocations act as obstacles, the mean free path is related to the dislocation density. Whether dislocations are either randomly distributed or organised into structures such as subgrains, the obstacle spacing is inversely proportional to the square root of dislocation density and hence $\Lambda \propto \rho^{-1/2}$. The effective mean free path should reflect the smallest of these microstructural length scales. Consequently, we follow Estrin (5) and calculate Λ using a harmonic mean

$$\frac{1}{\Lambda} = m\sqrt{\rho} + n\frac{1}{d}, \quad [3]$$

where m and n are material constants.

We now consider the annihilation processes of dynamic and static recovery. Dynamic recovery is the annihilation of dislocations associated with dislocation glide (3). During glide, a dislocation may pass near a dislocation of opposite sign, with which it can annihilate. Dynamic recovery is included as in the Kocks-Mecking-Estrin (KME) model (1, 3–5). Its parameterisation may be interpreted according to the framework of Essmann and Mughrabi (7), who assume that annihilation occurs when dislocations of opposite sign come within a critical distance y_c of each other. By modelling the probability that a moving dislocation will encounter a dislocation of opposite sign, the dynamic recovery rate can be calculated as

$$\dot{\rho}_{\text{dynamic}} = -\omega\rho|\dot{\varepsilon}| \quad [4]$$

where ω is a constant equal to $2y_c/b$ (8).

The KME model considers only storage and dynamic recovery. We extend this model with a parameterisation of static recovery, following the approach of Sandström (9). In contrast to Sandström, we emphasise the role of fast diffusion pathways. Static recovery is the time-dependent, endogenous process of dislocation annihilation. In this process, dislocation dipoles comprising dislocations of opposite sign are driven to climb and annihilate by the mutual attraction of their stress fields (10). Classically, static recovery follows second order kinetics (i.e. $\dot{\rho} \propto \rho^2$). Friedel (11, pp. 239) originally derived second order kinetics from detailed consideration of the spacing of a Frank network of dislocations. Blum (12) applied a more heuristic argument to derive the same kinetics. The rate of static recovery should scale with dislocation density divided by the timescale of an annihilation event. Blum showed that this timescale, which depends on the dislocation spacing and climb velocity, is inversely proportional to the dislocation density, such that static recovery follows second order kinetics. Dislocation climb is accommodated by the

diffusion of vacancies to the dislocation core and the climb velocity is proportional to the vacancy diffusivity. Therefore, the rate of static recovery is proportional to

$$\dot{\rho}_{\text{static}} \propto -D(T)\rho^2, \tag{5}$$

where $D(T)$ is the vacancy diffusivity, which we assume to have an Arrhenius dependence on temperature ((e.g., 10)).

While previous models typically assume that vacancies predominantly diffuse through the lattice, the relatively open structures of crystal defects such as dislocation cores and grain boundaries provide faster diffusion pathways. We refer to diffusion along these pathways as pipe diffusion and grain-boundary diffusion, respectively (13, 14). In olivine, dislocation structures are known to be anisotropic (15), which may result in an anisotropic diffusivity of crystal vacancies.

The simplest model of diffusivity that accounts for high-diffusivity pathways was proposed by Hart (16). Hart hypothesised that the effective diffusivity, accounting for both diffusion through the lattice and pipe diffusion, can be estimated as an average of the respective diffusivities of these pathways, weighted by volume fractions of the lattice ($f_{\text{lattice}} \approx 1$) and the dislocation cores ($f_{\text{pipe}} \approx \pi b^2 \rho$). Spingarn, Barnett, and Nix (13) performed a more detailed theoretical analysis confirming that Hart's is the relevant average for dislocation climb. Similarly, enhanced vacancy diffusivity in the vicinity of grain boundaries, due to grain-boundary diffusion, is assumed to increase the rate of dislocation climb (14). We include grain-boundary diffusion in our calculation of the effective diffusivity by assuming that the volume fraction of grain boundaries is $f_{\text{gb}} \approx 3\delta/d$, where δ is the grain boundary thickness. Increased rates of dislocation climb result in increased rates of static recovery. Consequently, accounting for the role and volume fraction of different diffusion pathways, we suggest the rate of static recovery is given by

$$\dot{\rho}_{\text{static}} = -\mathcal{R}_{\text{lattice}}(T)\rho^2 - \mathcal{R}_{\text{pipe}}(T)\rho^3 - \mathcal{R}_{\text{gb}}(T)\rho^2\frac{1}{d}, \tag{6}$$

where $\mathcal{R}_{\times}(T)$ are rate coefficients with an Arrhenius dependence on temperature as

$$\mathcal{R}_{\times}(T) = \mathcal{R}^*_{\times} \exp\left(-\frac{Q_{\times}}{RT}\right). \tag{7}$$

The activation energy, $Q_{\times}$, associated with each of these recovery mechanisms should reflect the underlying activation energy of the respective diffusion process.

Combining the terms for dislocation storage and recovery, our model is given by

$$\dot{\rho} = \underbrace{\frac{1}{b}\left(m\sqrt{\rho} + \frac{n}{d}\right)\dot{\varepsilon}}_{\text{storage}} - \underbrace{\omega\rho|\dot{\varepsilon}|}_{\substack{\text{dynamic}\\ \text{recovery}}} - \underbrace{\left(\mathcal{R}_{\text{lattice}}(T)\rho^2 + \mathcal{R}_{\text{pipe}}(T)\rho^3 + \mathcal{R}_{\text{gb}}(T)\rho^2\frac{1}{d}\right)}_{\text{static recovery}}. \tag{8}$$

Flow law. The flow law relates the strain rate due to dislocation motion to the applied stress. The strain rate depends on the density of moving dislocations and their velocity, expressed by the Orowan equation (17),

$$\dot{\varepsilon} = \rho_m b v, \tag{9}$$

where ρ_m is the density of mobile dislocations and v is the dislocation velocity. In the present theory, we do not distinguish between mobile and immobile dislocations. Instead, we make the simplifying assumption that the mobile dislocation density ρ_m is approximated by the total dislocation density ρ.

To derive an expression for the dislocation velocity, we follow the approach of Hansen et al. (18, 19). Dislocation motion involves the rearrangement of atomic bonds in a thermally activated process (20). Consequently, the rate of motion is proportional to a Boltzmann factor $\exp(-\Delta G/RT)$ with an activation energy $\Delta G(\sigma_{\text{eff}})$ that represents the energy barrier to be overcome for dislocation motion. In the presence of an effective stress σ_{eff}, the activation energy is reduced for motion of dislocations in the direction of the effective stress and increased for motion in the opposite direction (20). The directional stress dependence of the activation energy biases the motion of dislocations to be in the direction of the effective stress. We make the simplifying assumptions that the activation energy is linearly dependent on the effective stress, and that this linear dependence is equal and opposite in the forwards and reverse directions. The net velocity is proportional to the difference between the rates of forward and reverse motion. Consequently, the net velocity, as the difference between two exponential functions whose arguments have opposite sign, is proportional to the sinh of the effective stress (20, 21). The consideration of forward and reverse rates of motion led (18, 19) to obtain

$$v \propto \exp\left(-\frac{Q}{RT}\right)\sinh\left(\frac{Q}{RT}\frac{\sigma_{\text{eff}}}{\sigma^*_{\text{P}}}\right), \tag{10}$$

where Q is the activation energy in the absence of an effective stress, R is the ideal gas constant, T is the temperature, σ_{eff} is the effective stress, and σ^*_{P} is the strength of local barriers to dislocation motion. The assumption that the activation energy has a linear dependence on the effective stress is consistent with a model in which the local barrier to dislocation motion is lattice friction, as discussed by Hansen et al. (19). In this interpretation, σ^*_{P} is the Peierls stress. Substituting Eq. (10) for dislocation velocity into Eq. (9), the strain rate is given by

$$\dot{\varepsilon} = A(T)\rho\sinh\left(\frac{\sigma_{\text{eff}}}{\sigma_{\text{ref}}(T)}\right), \tag{11}$$

where $A(T)$ is a pre-factor with an Arrhenius dependence on temperature

$$A(T) = A^* \exp\left(-\frac{Q}{RT}\right), \quad [12]$$

and A^* is a pre-exponential constant. $\sigma_{\text{ref}}(T)$ is a temperature dependent reference stress that is given by

$$\sigma_{\text{ref}}(T) = \sigma_{\text{P}}^* \frac{RT}{Q}. \quad [13]$$

To make Eq. (11) useful in combination with the evolution of dislocation density of Eq. (8), we need to relate the effective stress to the applied stress.

The applied stress and the effective stress. The effective stress is a combination of the applied stress and internal stresses arising from the presence of dislocations and grain boundaries. To understand how these stresses contribute to the effective stress, we analyse our model in terms of non-equilibrium thermodynamics (22, 23). In this context, the second law of thermodynamics takes the form of the entropy inequality, which states that the rate of internal entropy production must be positive (24, 25). A process is thermodynamically admissible if it is compatible with the entropy inequality (25). We limit consideration to the internal entropy production rate associated with deformation, neglecting any potential coupling to other material processes (e.g., grain-size evolution). Consequently, the entropy inequality associated with our model is

$$\dot{\Sigma}^D = \frac{\sigma\dot{\varepsilon} - \gamma\dot{\rho}}{T} \geq 0, \quad [14]$$

where $\dot{\Sigma}^D$ is the internal entropy production rate associated with deformation. The energy per unit length of dislocation, γ, arises from the elastic strain of the lattice surrounding a dislocation and hence,

$$\gamma = c\mu b^2, \quad [15]$$

where c is a constant of order unity and μ is the elastic shear modulus (26, pp. 179–180). Substituting our model for $\dot{\rho}$ (Eq. (8)) into Eq. (14) and multiplying by T, the entropy inequality becomes

$$\left[\sigma - c\mu b\left(m\sqrt{\rho} + \frac{n}{d}\right)\right]\dot{\varepsilon} + \omega c\mu b^2 \rho|\dot{\varepsilon}| + c\mu b^2 \mathcal{R}_{\text{lattice}}(T)\rho^2 + c\mu b^2 \mathcal{R}_{\text{pipe}}(T)\rho^3 + c\mu b^2 \mathcal{R}_{\text{gb}}(T)\rho^2 \frac{1}{d} \geq 0. \quad [16]$$

Recovery terms act to reduce the dislocation density, and thus reduce the dislocation strain-energy density. As a result, the recovery terms in Eq. (16) are always associated with a positive source of entropy, and dislocation recovery processes are always compatible with the entropy inequality. In contrast, the first term is not necessarily associated with a positive entropy source. The entropy inequality, however, must hold for arbitrarily imposed deformations and dislocation densities, and so the strain rate dependent term must also be positive

$$\left[\sigma - c\mu b\left(m\sqrt{\rho} + \frac{n}{d}\right)\right]\dot{\varepsilon} \geq 0. \quad [17]$$

Substituting our derived flow law Eq. (11) for $\dot{\varepsilon}$, we find that

$$A(T)\rho\left[\sigma - c\mu b\left(m\sqrt{\rho} + \frac{n}{d}\right)\right]\sinh\left(\frac{\sigma_{\text{eff}}}{\sigma_{\text{ref}}(T)}\right) \geq 0. \quad [18]$$

Since $A(T)\rho$ is positive and sinh is an odd function of the effective stress, this inequality is satisfied if

$$\sigma_{\text{eff}} = \sigma - c\mu b\left(m\sqrt{\rho} + \frac{n}{d}\right), \quad [19]$$

thus defining the relationship between the applied stress σ and the effective stress. Although this relationship for the effective stress is sufficient to satisfy the entropy inequality, there are other, more non-linear relationships that would also satisfy it. However, experiments at both low and high temperatures support the linear relationship given in Eq. (19) (18, 19), and thus we use this relationship for the effective stress. We identify the second and third terms of this equation as the back stress σ_{b}, such that $\sigma_{\text{eff}} = \sigma - \sigma_{\text{b}}$. Back stress is the macroscopic quantity that summarises the cumulative effect of the internal stresses produced by elements of the microstructure. The back stress is

$$\sigma_{\text{b}} = \alpha\mu b\sqrt{\rho} + \beta\mu b\frac{1}{d}, \quad [20]$$

where $\alpha = cm$ and $\beta = cn$ are constants. The first term takes the form of the classical Taylor equation (27), which summarises the cumulative effect of stresses due to dislocation interactions. We therefore define this term to be the Taylor stress σ_ρ,

$$\sigma_\rho = \alpha\mu b\sqrt{\rho}. \quad [21]$$

We note that Thom et al. (28) have recently experimentally demonstrated that the Taylor relationship correctly describes back stresses in mineral single crystals.

The second term also takes a classical form, representing the stress within a grain of size d that must be exceeded by the applied stress for a dislocation loop to expand (29). We therefore define this term to be the threshold stress σ_d,

$$\sigma_d = \beta \mu b / d, \tag{22}$$

and assume that $|\sigma| > \sigma_d$ for dislocation-accommodated deformation to operate.
Using Eq. (20), the complete model is therefore given by

$$\dot{\rho} = \frac{1}{b}\left(m\sqrt{\rho} + \frac{n}{d}\right)\dot{\varepsilon} - \omega\rho|\dot{\varepsilon}| - \mathcal{R}_{\text{lattice}}(T)\rho^2 - \mathcal{R}_{\text{pipe}}(T)\rho^3 - \mathcal{R}_{\text{gb}}(T)\rho^2\frac{1}{d}, \tag{23}$$

$$\dot{\varepsilon} = A(T)\rho \sinh\left[\frac{\sigma - \sigma_{\text{b}}}{\sigma_{\text{ref}}(T)}\right]. \tag{24}$$

Once material parameters and grain size are specified, this system of two equations can be solved for the evolution of dislocation density and strain, given the applied stress.

Restatement of model in terms of Taylor stress. The model derived above determines the strain and dislocation-density rates in terms of the dislocation density, applied stress, and the back stress (the latter comprising the threshold and Taylor stresses). However, the dislocation density and the Taylor stress are related by the Taylor equation Eq. (21), and so one variable may be eliminated in favour of the other. Because the back stress may be inferred from measurements in a mechanical experiment, we eliminate the dislocation-density term in favour of the components of back stress (Taylor and threshold stress). This approach leads to

$$\dot{\sigma}_\rho = M\left(\frac{\sigma_\rho + \sigma_d}{\sigma_\rho}\dot{\varepsilon} - \frac{\sigma_\rho}{\sigma_{\rho,\max}}|\dot{\varepsilon}| - \mathcal{R}'_{\text{lattice}}(T)\sigma_\rho^3 - \mathcal{R}'_{\text{pipe}}(T)\sigma_\rho^5 - \mathcal{R}'_{\text{gb}}(T)\sigma_\rho^3\sigma_d\right), \tag{25}$$

$$\dot{\varepsilon} = A'(T)\sigma_\rho^2 \sinh\left(\frac{\sigma - \sigma_\rho - \sigma_d}{\sigma_{\text{ref}}(T)}\right), \tag{26}$$

where $M = cm^2\mu/2$ is a modulus associated with the evolution of Taylor stress and primes denote temperature-dependent factors whose pre-exponential factors have been redefined to absorb constants. We have introduced $\sigma_{\rho,\max}$, which, in the absence of a threshold stress represents an upper bound on the Taylor stress due to dynamic recovery. Dislocation storage and dynamic recovery, when framed in terms of the Taylor stress, take a similar form to the back stress model considered by Hansen et al. (18). Consequently, we can estimate some model parameters using the fitted constants from that previous study: the modulus M to be 135^{+55}_{-47} GPa and $\sigma_{\rho,\max}$ to be 1.8 ± 0.2 GPa.

Assumptions and simplifications. The full model of equations Eq. (25) and Eq. (26) is applicable at low temperature, for which dynamic recovery is more important, and high temperature, for which static recovery is dominant. Our interest in the present work is high-temperature deformation, hence we neglect the dynamic recovery term. Furthermore, we neglect recovery by lattice diffusion because it gives rise to a stress–strain-rate exponent of 3 and a stress–dislocation-density exponent of 2. Both of these exponents are inconsistent with laboratory measurements of olivine deformation (30).
In the calibration presented in the main text, we make the simplifying assumption that the activation energies and activation volumes of all processes are equal. The activation energies of pipe and grain-boundary diffusion are generally similar (31). Although our calibration using applied stresses, strain rates, and temperatures cannot robustly distinguish the different activation energies, any difference would lead to a temperature dependence of the relationship between dislocation density and applied stress. However, (15) clearly demonstrate that this relationship is not temperature dependent. Similarly, any difference in activation volumes between these processes would lead to a pressure dependence of this relationship, but (32) do not observe any pressure dependence. The absence of observations of a temperature or pressure dependence of the relationship between dislocation density and applied stress supports our assumption that these activation energies and activation volumes are at least very similar.
In this calibration, we have also neglected recovery controlled by lattice diffusion because the existing mechanical data from deformation experiments performed on olivine is insufficient to constrain it. The activation energy of lattice diffusion is expected to be 3/2 to 2 times bigger than the activation energies of fast diffusion. Consequently, it is possible that at higher temperatures and lower stresses, recovery controlled by lattice diffusion dominates over other recovery mechanisms. This recovery mechanism could be investigated in mechanical experiments performed at small stresses.
Moreover, since the focus of the present work is on understanding the consequences of dislocation-density evolution, we neglect temporal variations in mean grain size. These variations could be written in terms of an equation for $\dot{d}$, which would be coupled to Eq. (25) and Eq. (26) through the threshold stress σ_d. We defer this consideration to future work and simplify Eq. (25) to

$$\dot{\sigma}_\rho = M\left(\frac{\sigma_\rho + \sigma_d}{\sigma_\rho}\dot{\varepsilon} - \mathcal{R}'_{\text{pipe}}(T)\sigma_\rho^5 - \mathcal{R}'_{\text{gb}}(T)\sigma_\rho^3\sigma_d\right). \tag{27}$$

Solutions to this reduced equation are analysed in the main text, and explored in Figures 1 and 3.

The limit of large grain size. In the limit $\sigma_d \ll \sigma_\rho$ corresponding to large grain size (or the mechanical context of a single crystal), dislocation storage controlled by grain size and recovery controlled by grain-boundary diffusion are both negligible. Dropping these contributions from Eq. (26) and Eq. (27) leads to the grain-size-independent model

$$\dot{\sigma}_\rho = M\left[\dot{\varepsilon} - \mathcal{R}'_{\text{pipe}}(T)\sigma_\rho^5\right], \tag{28}$$

$$\dot{\varepsilon} = A'(T)\sigma_\rho^2 \sinh\left(\frac{\sigma - \sigma_\rho}{\sigma_{\text{ref}}(T)}\right). \tag{29}$$

In the main text we demonstrate that this model can explain canonical observations of dislocation creep in deformation of single crystals and polycrystalline samples with large grain size. It provides a good fit to the observed, steady-state stress–strain-rate relationship (Fig. 1A), stress–dislocation-density relationship (Fig. 1B) for olivine, as well as the evolution of strain rate under transient creep (Fig. 2A & 2B).

Determination of the Taylor constant. In the calibrated model, we eliminate dislocation density in favour of the Taylor stress. We can calculate the predicted steady-state Taylor stress at a given applied stress using Eq.'s 28 and 29. The dislocation density may then be calculated by rearranging the Taylor equation to yield

$$\rho = \left(\frac{\sigma_\rho(\sigma)}{\alpha\mu b}\right)^2. \tag{30}$$

However, α is an unknown constant that is not constrained during the model calibration with mechanical data. Instead, we calibrate α using observations of dislocation density at different applied stresses. Errors in the measurement of dislocation density are proportional to the dislocation density (33), and so we regress against the logarithm of dislocation density. As a result, we rearrange Eq. (30) to give

$$\log(\rho^i \mu b^2/\sigma_\rho(\sigma^i)) = -2\log(\alpha) + \epsilon^i, \tag{31}$$

where ϵ are observational errors that are assumed to be random, uncorrelated with zero mean, and the superscript i refers to the i^{th} observation, $i = 1 \ldots N$. The only unknown in Eq. (31) is intercept $-2\log(\alpha)$ and so Eq. (31) is an intercept-only model. The least squares estimate of $-2\log(\alpha)$ is therefore given by

$$-2\log(\alpha) = \frac{1}{N}\sum_{i=1}^{N} \log\left[\rho^i \mu b^2/\sigma_\rho(\sigma^i)\right]. \tag{32}$$

Using this approach, we calibrate α to be 2.46 ± 0.13. Importantly, the shape of the predicted dislocation-density–applied stress curve does not depend on the value of α. The calibrated value of α only has the effect of scaling the predicted dislocation-density by a constant value.

Transient creep solutions. We compare the predicted transient plastic strain following stress reductions to observations from Hansen et al. (19) in Figure 2. The experiments that we compare against were performed on single crystals. We therefore apply our model in the limit of infinite grain size. The single crystal used in the experiments plotted in Figure 2 was orientated in the $[101]_c$ direction. As olivine exhibits significant plastic anisotropy (34), the parameters that we have calibrated for polycrystalline aggregates do not apply to single crystals. Instead, we estimate these parameters using the observed data by rearranging Eq.'s 28 and 29 at steady state to obtain

$$A'(T) = \frac{\dot{\varepsilon}_0}{\sigma_{\rho,0}^2 \sinh\left(\frac{\sigma_0 - \sigma_{\rho,0}}{\sigma_{\text{ref}}(T)}\right)}, \tag{33}$$

$$\mathcal{R}'_{\text{pipe}}(T) = \frac{\dot{\varepsilon}_0}{\sigma_{\rho,0}^5}, \tag{34}$$

where $\dot{\varepsilon}_0$ is the steady-state strain rate prior to stress reduction, σ_0 is the applied stress prior to stress reduction, and $\sigma_{\rho,0}$ is the steady-state Taylor stress prior to stress reduction. Finally, we require the modulus M, which we estimate using Hansen et al.'s fitted parameters to be 26 GPa, for this crystallographic orientation.

The steady-state strain rate prior to reduction is observed to be $\dot{\varepsilon}_0 = 3.76 \times 10^{-5}$ s^{-1} at an applied stress $\sigma_0 = 162$ MPa. Hansen et al. estimate that the steady-state Taylor stress prior to reduction is $\sigma_{\rho,0} = 84$ MPa. However, we find that $\sigma_{\rho,0} = 104$ MPa better matches the transient strain-time curves.

Given $A'(T)$, $\mathcal{R}'(T)$, and M, we then numerically integrate Eq.'s 28 and 29 to obtain the predicted strain-time curves in Figure 2.

Prediction of the instantaneous viscosity change following a change in applied stress. Within our framework, the strain rate is given by

$$\dot{\varepsilon} = A(T)\rho \sinh\left(\frac{\sigma - \sigma_\rho - \sigma_d}{\sigma_{\text{ref}}(T)}.\right). \quad [35]$$

If the argument of the $\sinh(\cdot)$ term is small, it may be linearised as $\sinh(x) \approx x$. This linearisation is a good approximation for high-temperature, low applied stress deformation, and is especially applicable for deformation at geological conditions. Furthermore, in the instant following a change in the applied stress, the temperature, dislocation density, and grain size are unchanged, and therefore there is also no change in $\sigma_{\text{ref}}(T)$, σ_ρ, and σ_d. Thus, the ratio of strain rates immediately following ($\dot{\varepsilon}^+$) and prior to ($\dot{\varepsilon}^-$) the stress change are given by

$$\frac{\dot{\varepsilon}^+}{\dot{\varepsilon}^-} = \frac{\sigma^- + \Delta\sigma - \sigma_\rho - \sigma_d}{\sigma^- - \sigma_\rho - \sigma_d}, \quad [36]$$

where σ^- is the stress immediately prior to the stress change and $\Delta\sigma$ is the stress change. We now define the effective stress prior to the stress change as the difference between the applied stress and the sum of the Taylor and threshold stresses,

$$\sigma^-_{\text{eff}} = \sigma^- - \sigma_\rho - \sigma_d. \quad [37]$$

The magnitude of this variable is determined by the solution of the full model. Substituting this definition into Eq. (36), we obtain

$$\frac{\dot{\varepsilon}^+}{\dot{\varepsilon}^-} = \frac{\sigma^-_{\text{eff}} + \Delta\sigma}{\sigma^-_{\text{eff}}}. \quad [38]$$

Therefore, the ratio of viscosities immediately following (η^+) and prior to (η^-) the stress change is given by

$$\frac{\eta^+}{\eta^-} = \left(\frac{\sigma^- + \Delta\sigma}{\sigma^-}\right)\left(\frac{\dot{\varepsilon}^-}{\dot{\varepsilon}^+}\right), \quad [39]$$

$$= \left(1 + \frac{\Delta\sigma}{\sigma^-}\right)\left(\frac{\sigma^-_{\text{eff}}}{\sigma^-_{\text{eff}} + \Delta\sigma}\right). \quad [40]$$

If the stress change is small relative to the applied stress prior to the stress change, then

$$\frac{\eta^+}{\eta^-} \approx \frac{\sigma^-_{\text{eff}}}{\sigma^-_{\text{eff}} + \Delta\sigma}. \quad [41]$$

Consequently, the sensitivity of deformation to changes in the applied stress depends on the magnitude of the effective stress prior to the stress change relative to the stress change itself. If $\Delta\sigma \gg \sigma^-_{\text{eff}}$, then the instantaneous change in viscosity will be disproportionately large.

Approximate solution to step change in stress problem. In Figure 3C we present a numerical solution to the problem of a small step in applied stress from σ_0 to $\sigma_0 + \Delta\sigma$ at $t = 0$. Here, we derive an approximate solution to this problem by linear perturbation analysis.

Our calibrated model predicts that deformation at geological strain rates within the mantle is controlled by recovery facilitated by grain-boundary diffusion. In this limit, the model equations are

$$\dot{\varepsilon} = A'(T)\sigma_\rho^2 \sinh\left(\frac{\sigma - \sigma_\rho - \sigma_d}{\sigma_{\text{ref}}(T)}\right), \quad [42]$$

$$\dot{\sigma}_\rho = M\left(\frac{\sigma_\rho + \sigma_d}{\sigma_\rho}\dot{\varepsilon} - \mathcal{R}'_{\text{gb}}(T)\sigma_d\sigma_\rho^3\right). \quad [43]$$

We assume that at geological strain rates the stress difference $\sigma - \sigma_\rho - \sigma_d$ is small relative to the reference stress $\sigma_{\text{ref}}(T)$, such that we may assume $\sinh(x) \approx x$. Furthermore, mantle grain sizes are expected to be relatively large (e.g., 30), such that the threshold stress should be small relative to the applied stress. Consequently, we neglect terms proportional to the threshold stress σ_d except for the recovery term, which is required to balance Eq. (43) at steady state. Applying these simplifying assumptions, the model equations are

$$\dot{\varepsilon} = \frac{A'(T)}{\sigma_{\text{ref}}(T)}\sigma_\rho^2\left(\sigma - \sigma_\rho\right), \quad [44]$$

$$\dot{\sigma}_\rho = M\frac{A'(T)}{\sigma_{\text{ref}}(T)}\sigma_\rho^2(1+\zeta)\left(\frac{\sigma}{1+\zeta} - \sigma_\rho\right), \quad [45]$$

where $\zeta = \mathcal{R}'_{\rm gb}(T)\sigma_{\rm ref}(T)/A'(T)$ is a small parameter. The effective stress at steady-state is approximately $\sigma - \sigma_\rho \approx \zeta\sigma$. For geological conditions, $\zeta \ll 1$.

We now construct a series approximation for σ_ρ. Letting $\delta = \Delta\sigma/\sigma_0$, and expanding in δ, we find

$$\sigma = (1+\delta)\sigma_0, \tag{46}$$

$$\sigma_\rho = \sigma_{\rho,0} + \delta\sigma_{\rho,1}(t) + \delta^2\sigma_{\rho,2}(t) + \ldots. \tag{47}$$

Substituting this series into Eq. (45), we find to $\mathcal{O}(1)$ that

$$\sigma_{\rho,0} = \frac{\sigma_0}{1+\zeta}, \tag{48}$$

and to $\mathcal{O}(\delta)$ that

$$\dot\sigma_{\rho,1}(t) = M\frac{A'(T)}{\sigma_{\rm ref}(T)}\sigma_{\rho,0}^2(1+\zeta)\left(\frac{\sigma_0}{1+\zeta} - \sigma_{\rho,1}(t)\right), \tag{49}$$

which, together with the boundary condition that $\sigma_{\rho,1}(t=0) = 0$, has the solution

$$\sigma_{\rho,1}(t) = \frac{\sigma_0}{1+\zeta}\left(1 - \exp\left(-M\frac{A'(T)}{\sigma_{\rm ref}(T)}\frac{\sigma_0^2}{1+\zeta}t\right)\right). \tag{50}$$

Thus, to first order, the evolution of the Taylor stress is given by

$$\sigma_\rho = \frac{\sigma_0}{1+\zeta} + \frac{\Delta\sigma}{1+\zeta}\left(1 - \exp(-t/\tau)\right), \tag{51}$$

where the timescale τ is

$$\frac{1}{\tau} = M\frac{A'(T)}{\sigma_{\rm ref}(T)}\frac{\sigma_0^2}{1+\zeta}, \tag{52}$$

$$\approx M\frac{A'(T)}{\sigma_{\rm ref}(T)}\sigma_0^2. \tag{53}$$

The timescale of the transient τ is controlled by the flow law coefficient, and is insensitive to the recovery coefficient.

Over the course of the transient, the strain rate will change drastically, largely in response to changes in the effective stress. As a result, we neglect the effect of changes in the availability of dislocations to accommodate deformation, and focus on the evolution of the effective stress $\sigma - \sigma_\rho$. Consequently, using our approximation for the evolution of the Taylor stress, the strain rate is given by

$$\dot\varepsilon = \frac{A'(T)}{\sigma_{\rm ref}(T)}\left(\frac{\sigma_0+\Delta\sigma}{1+\zeta}\right)^2\left(\frac{\zeta}{1+\zeta}(\sigma_0+\Delta\sigma) + \frac{\Delta\sigma}{1+\zeta}\exp(-t/\tau)\right). \tag{54}$$

The predicted strain rate decays exponentially towards a steady state value. The first term corresponds to the steady-state strain rate following the transient. Substituting the definition of ζ, together with the assumption that $\zeta \ll 1$, we find that the strain rate in the limit of infinite time is

$$\dot\varepsilon_\infty \approx \mathcal{R}'_{\rm gb}(T)\sigma_d(\sigma+\Delta\sigma)^3, \tag{55}$$

which is sensitive to the recovery rate and independent of the flow law coefficient $A'(T)$. In contrast, the second term, which is the transient, excess strain rate above the background strain rate, is approximately

$$\dot\varepsilon_{\rm transient} \approx \frac{A'(T)}{\sigma_{\rm ref}(T)}(\sigma_0+\Delta\sigma)^2\Delta\sigma\exp(-t/\tau), \tag{56}$$

which is sensitive to the flow law coefficient, but independent of the recovery rate. An approximation for the excess plastic strain due to the transient can be found by integrating

$$\varepsilon_{\rm transient} = \int_0^\infty \dot\varepsilon_{\rm transient}\mathrm{d}t, \tag{57}$$

$$= \frac{A'(T)}{\sigma_{\rm ref}(T)}(\sigma_0+\Delta\sigma)^2\Delta\sigma\ \tau. \tag{58}$$

Substituting the definition of τ, and assuming that $\Delta\sigma \ll \sigma_0$, we find

$$\varepsilon_{\rm transient} \approx \frac{\Delta\sigma}{M}. \tag{59}$$

As the back-stress modulus M is similar in magnitude to the elastic modulus E (i.e. $M \approx E$), the transient occurs over a strain similar to the elastic strain $\Delta\sigma/E$ of the stress change.

Supplementary figures accompanying Figure 3C. To accompany Figure 3C in the main text, we examine the evolution of dislocation density following a step change in stress in Figure S1. The small stress increase leads to a similarly small increase in steady-state dislocation density. The dislocation density at depths between 100 and 200 km evolves over the course of approximately a year to a new steady state value. This range of depths for which dislocation density undergoes rapid evolution corresponds to the depths with the lowest viscosity in Figure 3C, reflecting the control of strain rate on dislocation density evolution. At depths shallower than 70 km, the dislocation density remains unchanged after 10 years. The dislocation density is frozen at its original value because temperatures are insufficiently high for dislocation storage or dislocation recovery.

In Figure S2, we examine the transient for the same stress change problem as a function of time at 100 km depth. In (A), the Taylor stress exponentially decays towards its new steady state value. The total change in Taylor stress is similar to the change in applied stress. In (B), we examine the dislocation-density evolution. The dislocation density is proportional to the square of the Taylor stress, and therefore it evolves to steady state over the same timescale. In (C), we plot the evolution of effective stress. Prior to the stress change, the effective stress is approximately 2 kPa. Immediately following the stress change, the effective stress is approximately 100 kPa, which decays away towards the new steady state value over half a year. The orders-of-magnitude change in effective stress is responsible for the orders-of-magnitude change in viscosity in Figure 3C. In (D), we plot the resultant change in strain rate. As the strain rate is proportional to the effective stress, the evolution of this variable mirrors (C). In (E), we plot the strain following the stress change. The strain increases rapidly up to a strain of $\approx 10^{-6}$, which is comparable to the predicted transient strain of $\Delta\sigma/M \approx 10^{-6}$. Following the transient, the strain increases at the background strain rate. In (F), we plot the Taylor stress as a function of strain. The change in Taylor stress is directly proportional to the strain, until the Taylor stress reaches its new steady state value. This linear relationship reflects the control of dislocation storage on transients at geological conditions.

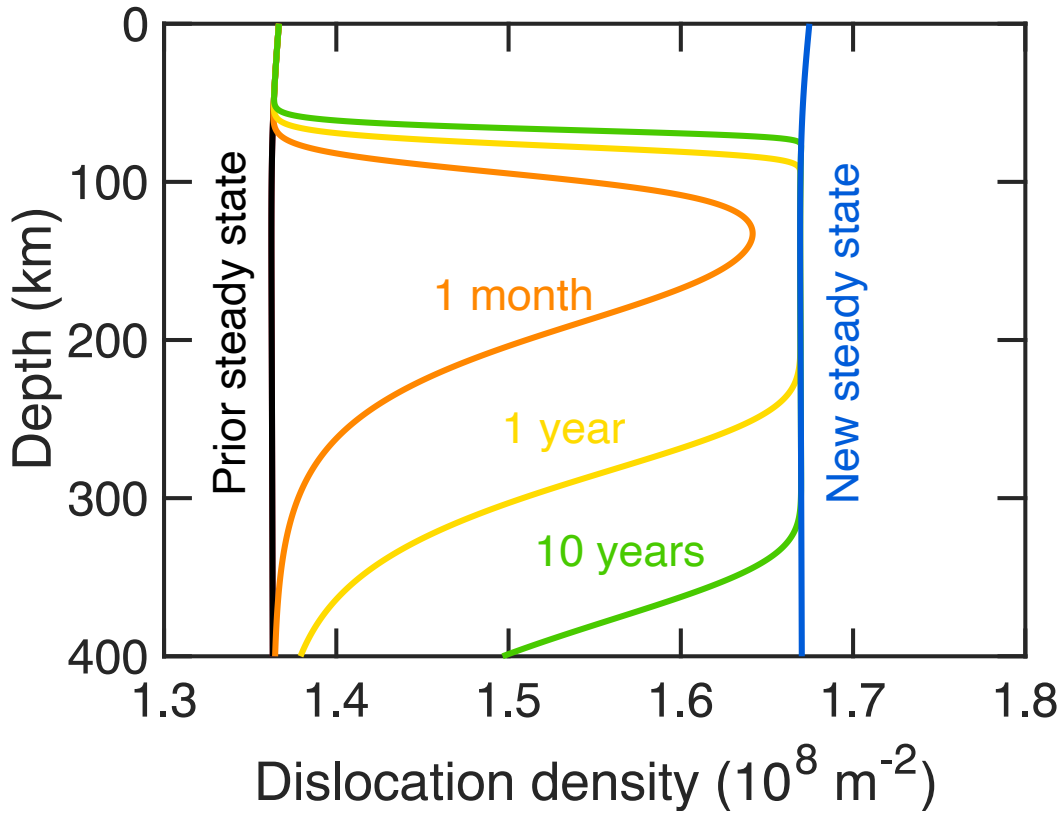

Fig. S1. Evolution of dislocation density following a step increase in stress from $1\,\mathrm{MPa}$ to $1.1\,\mathrm{MPa}$. The initial dislocation density is plotted as a black line. The colored lines indicate the dislocation density for a variety of times following the stress change (orange = 1 month, yellow = 1 year, green = 10 years). The new steady state dislocation density is indicated by the blue line. The grain size and temperature profile are the same as in Figure 3C.

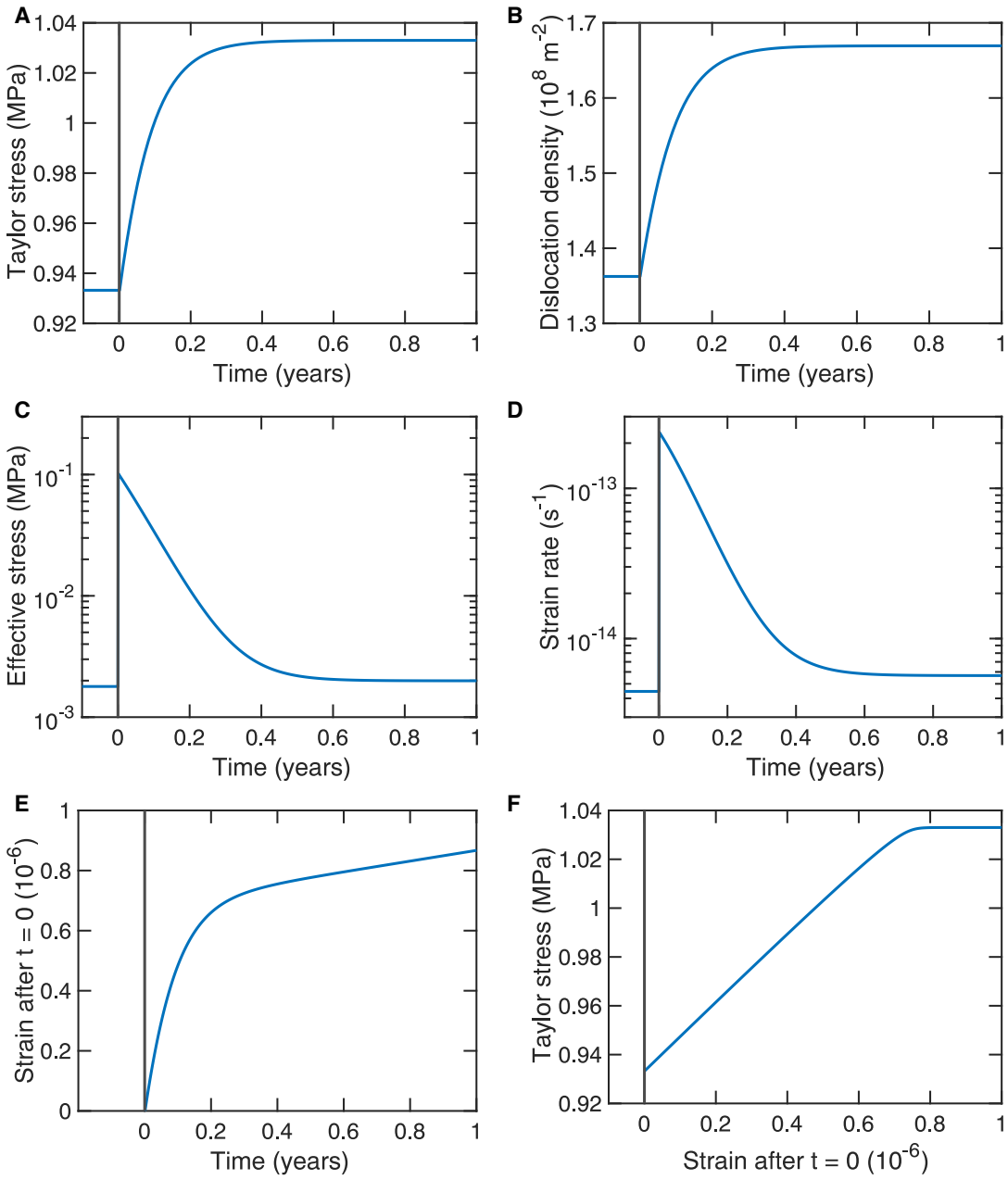

Fig. S2. The transient evolution of (A) Taylor stress, (B) dislocation density, (C) effective stress, (D) strain rate and (E) strain for the same conditions as in Figure 3C and Figure S1. For this figure, we examine the transient evolution at $100\,\mathrm{km}$ depth as an example. Transients at other depths will evolve similarly, but over different timescales. In (F), we plot the evolution of Taylor stress with strain after the stress change.

Model parameters.

Assumed values			
Parameter	Units	Value	Reference
μ	GPa	65	(15)
b	m	5×10^{-10}	(15)
β	-	2	(29)
σ_P^*	GPa	3.1 ± 0.4	(18)
M	GPa	135^{+55}_{-47}	(18)
ΔV	$cm^3 mol^{-1}$	15	(35)
Fitted values			
Parameter	Units	Pipe model (Fig. 1a)	Full model (Fig. 1c)
A'^*	$MPa^{-2} s^{-1}$	$10^{6.44 \pm 1.25}$	$10^{6.94 \pm 1.25}$
$\mathcal{R}'^*_{pipe}/A'^*$	MPa^{-3}	$10^{-6.43 \pm 0.45}$	$10^{-7.89 \pm 0.19}$
$\mathcal{R}'^*_{gb}/A'^*$	MPa^{-2}	N/A	$10^{-3.40 \pm 0.37}$
Q	kJ/mol	453 ± 37	450 ± 35
Inferred values$^{(\alpha)}$			
Parameter	Units	Pipe model (Fig. 1a)	Full model (Fig. 1c)
$\mathcal{R}'^*_{pipe}$	$MPa^{-5} s^{-1}$	$10^{0.01 \pm 1.38}$	$10^{-0.95 \pm 1.21}$
$\mathcal{R}'^*_{gb}$	$MPa^{-4} s^{-1}$	N/A	$10^{3.53 \pm 1.24}$
A^*	$m^2 s^{-1}$	$10^{-1.75 \pm 1.3}$	$10^{-1.26 \pm 1.3}$
$\mathcal{R}^*_{pipe}$	$m^4 s^{-1}$	$10^{-11.0 \pm 1.48}$	$10^{-11.9 \pm 1.32}$
$\mathcal{R}^*_{gb}$	$\mu m\ m^2 s^{-1}$	N/A	$10^{2.58 \pm 1.30}$

Table S1. Parameters from the calibrated model for olivine. Assumed values are taken from the literature. Fitted values are those directly constrained by the model calibration. Inferred values are calculated from the fitted values using the calibrated $\alpha = 2.46 \pm 0.13$. Where possible, the covariance matrix of the model calibration was used to estimate a 95% confidence interval. In the absence of a covariance matrix, confidence intervals were estimated using interval propagation. Superscript asterisks indicate the pre-exponential constant of a parameter assumed to have an Arrhenius dependence on temperature with Q. Primed variables are pre-exponential factors from the model in which dislocation density has been eliminated. The assumed activation volume ΔV is used for all of the Arrhenius terms in the model in the construction of Figure 3C.

References

1. H Mecking, U Kocks, Kinetics of flow and strain-hardening. *Acta Metall.* **29**, 1865–1875 (1981).
2. U Kocks, A statistical theory of flow stress and work-hardening. *Philos. Mag.* **13**, 541–566 (1966).
3. UF Kocks, Laws for Work-Hardening and Low-Temperature Creep. *J. Eng. Mater. Technol.* **98**, 76–85 (1976).
4. Y Estrin, H Mecking, A unified phenomenological description of work hardening and creep based on one-parameter models. *Acta Metall.* **32**, 57–70 (1984).
5. Y Estrin, Dislocation theory based constitutive modelling: foundations and applications. *J. Mater. Process. Technol.* **80**, 33–39 (1998).
6. W Blum, P Eisenlohr, Dislocation mechanics of creep. *Mater. Sci. Eng. A* **510**, 7–13 (2009).
7. U Essmann, H Mughrabi, Annihilation of dislocations during tensile and cyclic deformation and limits of dislocation densities. *Philos. Mag. A* **40**, 731–756 (1979).
8. E Nes, K Marthinsen, Y Brechet, On the mechanisms of dynamic recovery. *Scripta Materialia* **47**, 607–611 (2002).
9. R Sandström, J Hallgren, The role of creep in stress strain curves for copper. *J. nuclear materials* **422**, 51–57 (2012).
10. W Nix, J Gibeling, D Hughes, Time-dependent deformation of metals. *Metall. Transactions A* **16**, 2215–2226 (1985).
11. J Friedel, *Dislocations*, Addison-Wesley series in metallurgy and materials. (Pergamon ; [Distributed in USA by] Addison-Wesley Pub. Co, Oxford : Reading, Mass), Reprinted with corrections edition, (1964).
12. W Blum, Role of dislocation annihilation during steady-state deformation. *Phys. Status Solidi (b)* **45**, 561–571 (1971).
13. J Spingarn, D Barnett, W Nix, Theoretical descriptions of climb controlled steady state creep at high and intermediate temperatures. *Acta Metall.* **27**, 1549–1561 (1979).
14. J Spingarn, W Nix, A model for creep based on the climb of dislocations at grain boundaries. *Acta Metall.* **27**, 171–177 (1979).
15. Q Bai, D Kohlstedt, High-temperature creep of olivine single crystals, 2. dislocation structures. *Tectonophysics* **206**, 1–29 (1992).
16. E Hart, On the role of dislocations in bulk diffusion. *Acta Metall.* **5**, 597 (1957).
17. E Orowan, Zur kristallplastizität. i. *Zeitschrift für Physik* **89**, 605–613 (1934).
18. LN Hansen, et al., Low-temperature plasticity in olivine: Grain size, strain hardening, and the strength of the lithosphere. *J. Geophys. Res. Solid Earth* **124**, 5427–5449 (2019).
19. LN Hansen, D Wallis, T Breithaupt, CA Thom, I Kempton, Dislocation creep of olivine: Backstress evolution controls transient creep at high temperatures. *J. Geophys. Res. Solid Earth* **126**, e2020JB021325 (2021).
20. A Krausz, A rate theory of dislocation mobility. *Acta Metall.* **16**, 897–902 (1968).

21. X Wu, A Krausz, A kinetics formulation for low-temperature plasticity. *J. materials engineering performance* **3**, 169–177 (1994).
22. D Jou, J Casas-Vázquez, G Lebon, Extended irreversible thermodynamics. *Ext. Irreversible Thermodyn.* pp. 41–74 (1996).
23. G Lebon, D Jou, J Casas-Vázquez, *Understanding non-equilibrium thermodynamics.* (Springer) Vol. 295, (2008).
24. I Müller, On the entropy inequality. *Arch. for Ration. Mech. Analysis* **26**, 118–141 (1967).
25. BD Coleman, W Noll, The thermodynamics of elastic materials with heat conduction and viscosity in *The Foundations of Mechanics and Thermodynamics.* (Springer), pp. 145–156 (1974).
26. JP Hirth, J Lothe, *Theory of dislocations.* (Wiley, New York ; Chichester), 2nd ed edition, (1982).
27. GI Taylor, The mechanism of plastic deformation of crystals. part i.—theoretical. *Proc. Royal Soc. London. Ser. A, Containing Pap. a Math. Phys. Character* **145**, 362–387 (1934).
28. CA Thom, LN Hansen, T Breithaupt, DL Goldsby, KM Kumamoto, Backstresses in geologic materials quantified by nanoindentation load-drop experiments. *Philos. Mag.* pp. 1–15 (2022).
29. TT Gribb, RF Cooper, Low-frequency shear attenuation in polycrystalline olivine: Grain boundary diffusion and the physical significance of the andrade model for viscoelastic rheology. *J. Geophys. Res. Solid Earth* **103**, 27267–27279 (1998).
30. G Hirth, D Kohlstedt, The stress dependence of olivine creep rate: Implications for extrapolation of lab data and interpretation of recrystallized grain size. *Earth Planet. Sci. Lett.* **418**, 20–26 (2015).
31. HJ Frost, MF Ashby, *Deformation mechanism maps: the plasticity and creep of metals and ceramics.* (Pergamon press), (1982).
32. T Ohuchi, Si Karato, K Fujino, Strength of single-crystal orthopyroxene under lithospheric conditions. *Contributions to Mineral. Petrol.* **161**, 961–975 (2011).
33. R Farla, et al., Dislocation recovery in fine-grained polycrystalline olivine. *Phys. Chem. Miner.* **38**, 363–377 (2011).
34. Q Bai, S Mackwell, D Kohlstedt, High-temperature creep of olivine single crystals 1. mechanical results for buffered samples. *J. Geophys. Res. Solid Earth* **96**, 2441–2463 (1991).
35. NA Dixon, WB Durham, Measurement of activation volume for creep of dry olivine at upper-mantle conditions. *J. Geophys. Res. Solid Earth* **123**, 8459–8473 (2018).